

Multifield Induced Antiferromagnet Transformation into Altermagnet and Realized Anomalous Valley Hall Effect in Two-dimensional Materials

Hanbo Sun,¹ Pengqiang Dong,¹ Chao Wu,¹ and Ping Li^{1,2,3,*}

¹*State Key Laboratory for Mechanical Behavior of Materials, School of Materials Science and Engineering, Xi'an Jiaotong University, Xi'an, Shaanxi, 710049, People's Republic of China*

²*State Key Laboratory of Silicon and Advanced Semiconductor Materials, Zhejiang University, Hangzhou, 310027, People's Republic of China*

³*State Key Laboratory for Surface Physics and Department of Physics, Fudan University, Shanghai, 200433, People's Republic of China*

(Dated: February 26, 2025)

Altermagnetism, as a new category of collinear magnetism distinct from traditional ferromagnetism and antiferromagnetism, exhibits the spin splitting without net magnetization. Currently, researchers are focus on searching three-dimensional altermagnetism and exploring its novel physical properties. However, there is a lack of understanding of the physical origin of two-dimensional altermagnetic emergent behavior. Here, we propose an approach to realize the transition from Neel antiferromagnetism to altermagnetism in two-dimensional system using an electric field, Janus structure, and ferroelectric substrate. In monolayer VPSe₃, we demonstrate that multiple-physical-fields cause the upper and lower Se atoms unequal to break *PT* symmetry, resulting in altermagnetic spin splitting. Noted that monolayer VPSe₃ produces a spontaneous valley splitting of 2.91 meV at the conduction band minimum. The electric field can effectively tune the valley splitting magnitude, while the Janus structure not only changes the valley splitting magnitude, but also alters the direction. More interestingly, when the ferroelectric polarization of Al₂S₃ is P \uparrow , the direction of valley polarization is switched and the magnitude is almost unchanged. However, the valley splitting significantly increases under the P \downarrow . It is worth noting that the ferroelectric polarization can switch altermagnetic effect and realize anomalous valley Hall effect. Besides, we reveal the microscopic mechanism of valley splitting by an effective Hamiltonian. Our findings not only provide a method to designing altermagnet, but also enriches the valley physics.

I. INTRODUCTION

Recently, a new type of magnetism named "altermagnetism" has been proposed in condensed matter physics [1–5]. The altermagnetism has two fascinating properties, which mainly manifested as a zero net magnetic moment and spin splitting along specific high symmetry paths without the spin-orbit coupling (SOC). The discovery has not only promoted the development of spintronics, but also enriched the application scenarios of magnetic materials. For example, giant and tunneling magnetoresistance effect is raised in altermagnets [6]. Besides, the anomalous Hall effect is reported in the altermagnet RuO₂, which the magnitude can be compared to that of ferromagnet (FM) [7]. In addition, a new type of torque, spin splitter torque, has been theoretically proposed [8] and experimentally observed [9, 10] in the altermagnet. Moreover, the heterojunctions of altermagnet are reported to possess chiral Majorana Fermion or Majorana zero energy modes [11, 12]. However, these investigations have mainly focused on bulk materials [2–10, 13–16], while two-dimensional (2D) altermagnets pay limited attention. How to tune the 2D antiferromagnet (AFM) into altermagnet is even less involved. But it is crucial to understanding the origin of the emergent be-

havior.

In spintronics, a new degree of freedom, valley, has been proposed as the third degree of freedom beyond the electron's charge and spin [17–20]. The valley indicates a local energy minimum or maximum point in the conduction or valence band. At present, the investigation focus of valleytronics is how to realize spontaneous valley polarization and effectively tune [21–29]. There are two main ways to achieve spontaneous valley polarization, which is named ferrovalley material [21]. One approach is to break the time-reversal symmetry (*T*) with the FM or AFM [21–25, 29], while the other way is to break the inversion symmetry (*P*) by ferroelectricity [27, 28, 30]. It is well known that altermagnets break the combined symmetry of the *P* and *T* (named the *PT* symmetry). Whether the altermagnetism can realize spontaneous valley polarization, and how it differs from the FM and AFM systems?

In this work, we propose a new scheme for achieving altermagnetism in 2D system. Here, we focus on the transformation of AFM into altermagnet by the multifield induction, such as an electric field, Janus structure, and ferroelectric substrate. It is well known that the AFM hold the *PT* symmetry. The multiple-physical-fields can induce the *PT* symmetry breaking, which causes the band degeneracies of spin up and spin down bands to disappear on special high symmetrical path, exhibiting altermagnetic characteristics. Based on the density functional theory (DFT) calculations, we demonstrate this mech-

* pli@xjtu.edu.cn

anism and phenomena in monolayer VPSe_3 . Moreover, monolayer VPSe_3 exhibits spontaneously valley polarization due to the combined effects of SOC and T symmetry breaking. The electric field can effectively tune the magnitude of valley splitting, while the Janus structure (built-in electric field) and ferroelectric substrate can regulate not only the magnitude but also the direction and position of valley polarization. In addition, the ferroelectric polarization can switch altermagnetic effect and realize anomalous valley Hall effect. Our work provide a new direction for investigating altermagnetism and valleytronic devices.

II. STRUCTURES AND COMPUTATIONAL METHODS

Based on the framework of the DFT, we employed the Vienna *Ab initio* simulation package (VASP) [31, 32] to investigate the electronic and magnetic properties. The generalized gradient approximation (GGA) with the Perdew-Burke-Ernzerhof (PBE) functional is used to describe the exchange correlation energy [33]. The kinetic energy cutoff for plane-wave basis is set to be 500 eV. A vacuum of 30 Å is added along the c -axis, to avoid the interaction between the sheet and its periodic images. The convergence criteria of the total energy and the force for lattice optimization are set to 10^{-6} eV and -0.005 eV/Å, respectively. To describe strongly correlated $3d$ electrons of V, the GGA+U approach is performed with the effective U value ($U_{eff} = U - J$) of 3 eV [34]. The zero damping DFT-D3 approach of Grimme is considered for the van der Waals (vdW) correction in $\text{VPSe}_3/\text{Al}_2\text{S}_3$ heterostructure [35]. In addition, to study the Berry curvature, the maximally localized Wannier functions (MLWFs) are used to construct an effective tight-binding Hamiltonian by Wannier90 code [36, 37].

III. RESULTS AND DISCUSSION

IV. RESULTS AND DISCUSSION

A. Structure and symmetry

As shown in Fig. 1(a), it shows the crystal structure of monolayer VPSe_3 , which is six Se atom nearest to each V atom. The monolayer VPSe_3 shows a hexagonal honeycomb lattice with the point group of D_{3d} and space group of $P\bar{3}1m$. The optimized lattice constant of VPSe_3 is 6.24 Å. When magnetic order isn't considered, monolayer VPSe_3 has the P symmetry. However, since the magnetic ground state of VPSe_3 is Néel AFM, both the P and T symmetry are broken. Despite this, it exhibits invariance when the spatial inversion and time reversal occur simultaneously, that is, the PT symmetry (see Fig. 1(b)). It is well established that a system with PT symmetry exhibits Kramers degeneracy in its band structure.

Namely, as shown in Fig. 1(c), the spin up and spin down bands are degenerate. Besides, the opposite spin sublattices are jointed by the combined rotation and mirror symmetry, denoted as $[C_2||M]$. The $[C_2||M]$ symmetry lead to $E(s, \mathbf{k}) = [C_2||M]E(s, \mathbf{k}) = E(-s, M\mathbf{k})$, which plays a vital role in realizing altermagnetism. Here, the s , \mathbf{k} , and $E(s, \mathbf{k})$ represent the spin, momentum, and spin- and momentum-dependent bands, respectively.

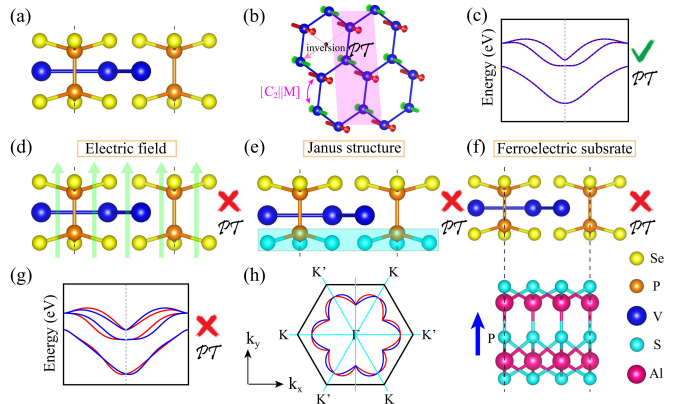


FIG. 1. (a) The side view of the crystal structure for monolayer VPSe_3 . (b) Schematic diagram of Néel type magnetic order for monolayer VPSe_3 with the PT symmetry. (c) Band structure of AFM-N state with the PT symmetry. Three kinds of field induced PT symmetry breaking. (d) Applied an external electric field. (e) Functionalizing the crystal structure into Janus configuration form by substituting the bottom Se layer through S atoms. (f) Ferroelectric substrate is introduced to form vdW heterostructure. (g) Band structure of AFM-N state with broken the PT symmetry. (h) The band structures shows i-wave symmetry without the SOC effect. The magenta, the light blue, blue, orange, and yellow balls represent Al, S, V, P, and Se elements, respectively.

Here, we propose three kinds of field to break the PT symmetry. As shown in Fig. 1(d-f), these include the application of out-of-plane external electric fields, the functionalizing crystal structure into Janus configuration form by substituting the bottom Se layer through S atoms, and the applied ferroelectric substrate. A common feature of these three methods is that the mirror symmetry can be preserved. Consequently, as shown in Fig. 1(g), the Kramers degeneracy is lifted, and the band structure characteristics of altermagnet are exhibited. More interestingly, as shown in Fig. 1(h), the i-wave altermagnets are formed.

B. Band structure and valley splitting

To determine the magnetic ground state of monolayer VPSe_3 , the two most likely magnetic configurations including the FM and Neel type AFM are considered (the Neel Type AFM is hereinafter referred to as AFM). We calculate that the FM state is 277.67 meV more energy

than the AFM state, which indicates that the AFM phase is the magnetic ground state of monolayer VPSe₃. For the 2D magnetic materials, the out-of-plane magnetic anisotropy energy (MAE) is the basis for their stable existence [38, 39]. The MAE is defined as MAE = E₁₀₀ - E₀₀₁, where E₁₀₀ and E₀₀₁ represent the total energy of the magnetic moment along [100] and [001] axis, respectively. The calculated MAE is 0.10 meV, which indicates the easy magnetization direction along the [001] axis.

Then, we calculate the spin-polarized band structure of monolayer VPSe₃. As shown in Fig. 2(a), the spin up and spin down bands are degenerate, which the *PT* symmetry induces the Kramers degeneracy. It is worth noting that the K/K' valley of conduction band minimum (CBM) is degenerate. Noted that Fig. 2(c) plots the valence band at around -1.2 eV. When the SOC is switched on, as shown in Fig. 2(b), the energy valley degeneracy of K and K' disappears, resulting in 2.91 meV spontaneous valley splitting. Here, we define valley splitting as the energy difference between K and K' points. The origin of valley splitting in monolayer VPSe₃ is consistent with the previously reported magnetic system due to the combined *T* symmetry broken and SOC effect. To understand the orbital composition of valley splitting, we calculate the orbital-resolved band structure of monolayer VPSe₃. As shown in Fig. S1, the valence band maximum (VBM) bands are mainly contributed by the d_{x²-y²}+d_{xy}+d_{z²} orbitals of V atoms, while the CBM bands are dominated by the p_x+p_y orbitals of Se atoms.

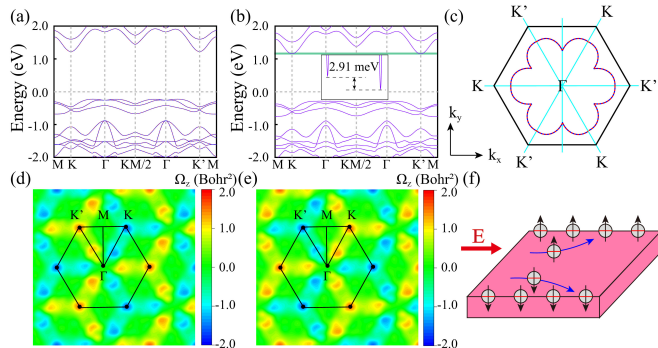


FIG. 2. (a) Spin-polarized band structure of monolayer VPSe₃. The solid red line and dashed blue line represent spin up and spin down bands, respectively. (b) The band structures with the SOC effect. The valley splitting of conduction band is exhibited by the green shading. (c) The valence band at around -1.2 eV. The Berry curvatures of monolayer VPSe₃ for (d) spin up state, and (e) spin down state in the entire Brillouin zone. (f) Schematic diagram of spin-valley Hall effect in the electron-doped monolayer VPSe₃ at the K' valley. The electrons and holes are shown by the - and + symbol. The \uparrow and \downarrow represents the spin up and spin down carriers, respectively.

To understand the origin of valley splitting in monolayer VPSe₃, we employed $|\psi_c^\tau\rangle = \frac{1}{\sqrt{2}}(|p_x\rangle + i\tau|p_y\rangle) \otimes |\uparrow\rangle$ as the orbital basis to build an effective Hamiltonian. The

$\tau = \pm 1$ represent the valley index referring to the K/K' point. Taken the SOC effect as a perturbation term, the effective Hamiltonian can be written as

$$\hat{H}_{SOC} = \lambda \hat{S} \cdot \hat{L} = \hat{H}_{SOC}^0 + \hat{H}_{SOC}^1, \quad (1)$$

where \hat{S} and \hat{L} are spin and orbital angular operators, respectively. The \hat{H}_{SOC}^0 and \hat{H}_{SOC}^1 denote the interaction between the same spin states and between opposite spin states, respectively. In monolayer VPSe₃, we only consider the interaction between spin up states. Thus, the \hat{H}_{SOC}^1 term can be neglected. Accordingly, the \hat{H}_{SOC}^0 can be rewritten by polar angles

$$\hat{H}_{SOC}^0 = \lambda \hat{S}_{z'} (\hat{L}_z \cos\theta + \frac{1}{2} \hat{L}_+ e^{-i\phi} \sin\theta + \frac{1}{2} \hat{L}_- e^{+i\phi} \sin\theta), \quad (2)$$

When the easy magnetization axis is along the out-of-plane, $\theta = \phi = 0^\circ$, then the \hat{H}_{SOC}^0 term can be reduced as

$$\hat{H}_{SOC}^0 = \lambda \hat{S}_z \hat{L}_z, \quad (3)$$

Therefore, the energy level of the CBM valley can be written as $E_c^\tau = \langle \psi_c^\tau | \hat{H}_{SOC}^0 | \psi_c^\tau \rangle$. Consequently, the valley splitting can be described as

$$E_c^K - E_c^{K'} = i \langle p_x | \hat{H}_{SOC}^0 | p_y \rangle - i \langle p_y | \hat{H}_{SOC}^0 | p_x \rangle \approx \lambda, \quad (4)$$

where the $\hat{L}_z |p_x\rangle = i\hbar |p_y\rangle$, $\hat{L}_z |p_y\rangle = -i\hbar |p_x\rangle$.

In addition, we understand valleys in terms of Berry curvature. Since monolayer AFM VPSe₃ is protected by *PT* symmetry, the Berry curvature is zero for the entire Brillouin zone. Therefore, we calculate the Berry curvature of spin up and spin down states. As shown in Fig. 2(d, e), the Berry curvature has equal magnitude at the K and K' points, while it shows opposite signs for the same valley of different spin states and different valleys of the same spin state. When the Fermi level shifts the conduction band of K' valley by electron doping, the spin up electrons from K' valley will be accumulated at the right edge of the sample, while the spin down electrons from K' valley will shift to the left edge under an in-plane electric field. As shown in Fig. 2(f), we name the phenomenon the spin-valley Hall effect.

C. Electric field induce transformation into altermagnet

From the perspective of device applications, the electric field stands out as the most effective means for tuning the physical quantity [40, 41]. This modulation method not only responds swiftly but also avoids causing damage to the materials themselves, demonstrating unique advantages in the application of micro- and nano-devices. Therefore, we investigate the effect of electric field on monolayer VPSe₃. Here, instead of re-optimizing VPSe₃ structure, we apply an electrostatic potential to monolayer VPSe₃. This causes the upper and lower Se atomic

layer to be inequivalent, resulting in the broken PT symmetry. In the absence of the SOC effect, the band structure holds sixfold rotational symmetry (C_6). The $E(s, \mathbf{k}) = E(-s, -\mathbf{k})$ relationship is satisfied on special high symmetric lines. However, the rotational symmetry of band structure will be reduced to threefold (C_3) under the SOC effect.

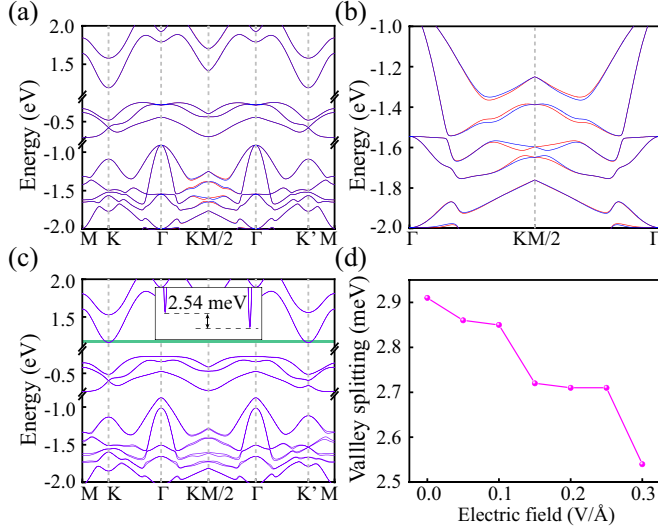


FIG. 3. (a) Spin-polarized band structure of monolayer $VPSe_3$ under an external electric field of 0.3 V/\AA . The solid red and blue lines denote spin up and spin down bands, respectively. (b) An enlarged view of the region around $KM/2$ in (a). (c) The band structures with the SOC effect under an external electric field of 0.3 V/\AA . The valley splitting of conduction band is shown by the green shading. (d) The valley splitting of monolayer $VPSe_3$ as a function of the external electric field.

Firstly, we investigate the magnetic ground state at the $0.0 \sim 0.3 \text{ V/\AA}$. As shown in Fig. S2, the effect of electric field on the energy difference between FM and AFM states is only 0.1 meV , which means that the AFM phase is still the magnetic ground state. To confirm the symmetry analysis, we calculate the band structure at an electric field of 0.3 V/\AA . As shown in Fig. 3(a), both valence and conduction bands of the valley at K and K' points are completely degenerate, which verifies that the band structure has C_6 symmetry without the SOC effect. More interestingly, as shown in Fig. 3(b), the spin splitting exhibits at the Γ - $KM/2$ - Γ path. It is the typical characteristic of altermagnet, which the AFM material doesn't have. Moreover, when the SOC is included, the valley splitting of 2.54 meV is still observed at the CBM. Since the valley degeneracy of K and K' points disappears, the symmetry decreases from the C_6 to C_3 . It also demonstrates our symmetry analysis. Besides, as shown in Fig. 3(d), the change of valley splitting is only 0.4 meV at the $0.0 \sim 0.3 \text{ V/\AA}$. It is mainly because the splitting valley is contributed by the non-magnetic Se atom.

D. Janus structure induce transformation into altermagnet

The second approach is that it actually makes the upper and lower Se atomic layers unequal. We use S atom to replace lower Se atom to form the Janus structure $V_2P_2S_3Se_3$. To enrich the physical properties of 2D materials, Zhang *et al.* has successfully prepared Janus graphene as early as 2013 [42]. After more than ten years of development, the current technology for preparing 2D Janus structures has been very mature and successfully synthesized Janus transition metal dichalcogenides (TMDs), such as $MoSSe$ [43], $WSSe$ [44], Janus MXenes [45] etc. Due to the asymmetry between the lower and upper surfaces of the Janus structure, a significant built-in electric field is produced. Therefore, it naturally breaks the PT symmetry. We speculate that the same phenomenon of $VPSe_3$ applied electric field will be generated in $V_2P_2S_3Se_3$.

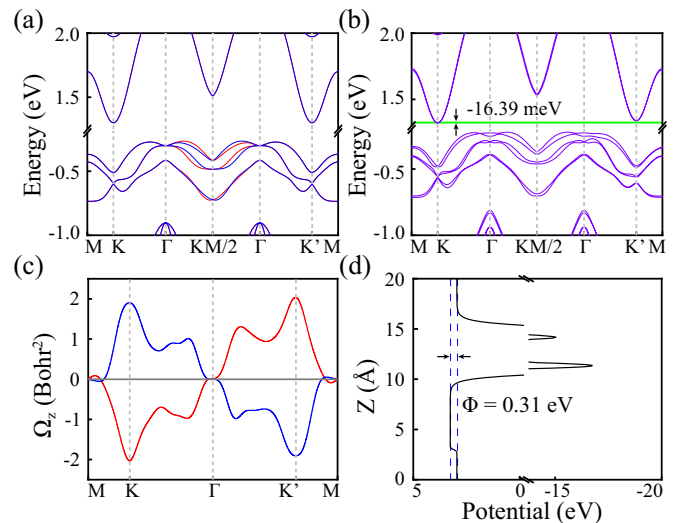


FIG. 4. (a) Spin-polarized band structure of Janus $V_2P_2S_3Se_3$. The solid red and blue lines represent spin up and spin down bands, respectively. (b) The band structures of Janus $V_2P_2S_3Se_3$ with the SOC effect. The valley splitting of conduction band is exhibited by the green shading. (c) The Berry Curvature along the high symmetry line. The red and blue lines represent Berry Curvatures of spin up and spin down states, respectively. (d) The planar averaged electrostatic potential of Janus $V_2P_2S_3Se_3$.

In the absence of SOC, as shown in Fig. 4(a), the significant spin splitting is clearly observed in the Γ - $KM/2$ - Γ path. It indicates that the AFM to altermagnet transition is realized by constructing the Janus structure without the PT symmetry. In addition, the CBM at the K and K' points exhibits valley degeneracy. When the SOC is switched on, as illustrated in Fig. 4(b), the K and K' valley degeneracies disappear, producing valley splitting up to -16.39 meV . It demonstrates that the intrinsic spontaneous valley polarization is achieved in the altermagnet

monolayer $V_2P_2S_3Se_3$. Besides, to understand the valley related physics, we calculate Berry curvature of the monolayer $V_2P_2S_3Se_3$. As shown in Fig. 4(c), the Berry curvature of spin up exhibits a negative value near the K point and a positive near the K' point. On the contrary, the Berry curvature of spin down is completely reversed sign. It is also the characteristic of valley degeneracy. To further understand the valley splitting of monolayer $V_2P_2S_3Se_3$ -16.39 meV, we introduce the built-in electric field $E_{in} = (\Phi_2 - \Phi_1)/\Delta h$, where Φ_1 , Φ_2 , and Δh represent the electrostatic potential at the upper surface and lower surface, and structural height of $V_2P_2S_3Se_3$, respectively. As shown in Fig. 4(d), the built-in electric field is 0.10 V/Å by the electrostatic potential. The built-in electric field of 0.10 V/Å not only significantly increases the valley splitting, but also changes its sign. Why is the regulation effect of 0.10 V/Å built-in electric field on valley splitting much better than that of external electric field. The important reason is the difference in SOC strength between S and Se atoms, which the S and Se atoms are 1.8 meV and 4.0 meV, respectively.

E. Ferroelectric substrate induce transformation into altermagnet

A third method to achieve altermagnets is by constructing heterostructures, which the heterostructure is naturally broken PT symmetry. In order to explore the regulation of substrate on valley splitting, we choose the ferroelectric substrate Al_2S_3 and $VPSe_3$ to form heterostructure. The lattice constant of Al_2S_3 is 3.59 Å. We find that the lattice mismatch rate of the 1×1 unit cell of $VPSe_3$ matching the $\sqrt{3} \times \sqrt{3}$ Al_2S_3 is only 0.3%. As shown in Fig. 5(a, e) and Fig. S3, four typical configurations are considered: top-S, top-Al, bridge, and hollow configuration. As listed in Table SI, the layer spacing in all configurations is 3.24 ~ 3.82 Å, which indicates the interlayer is typically weak vdW interaction. In addition, all configurations exhibit an out-of-plane MAE, as listed in Table SII. From the relative total energy in Table SIII, the top-S, and top-Al are the most stable $P\uparrow$ and $P\downarrow$ configurations, respectively.

In the following, we take top-S configuration as an example for detailed analysis. When the ferroelectric polarization of Al_2S_3 is $P\uparrow$, the spin-polarized band structure is illustrated in Fig. 5(b). The VBM and CBM are located at K- Γ path and K/K' point, simultaneously, the CBM of K and K' points exhibit valley degeneracy. When the $P\uparrow$ switches $P\downarrow$, as shown in Fig. 5(f), the CBM becomes the M point, while the VBM remains on the K- Γ path. Very interestingly, the valley of VBM shows degeneracy, which is not a high symmetric point. Most importantly, as shown in Fig. 5(c, g), both $P\uparrow$ and $P\downarrow$ configurations produce spin splitting. This confirms the feasibility of our mechanism for realizing altermagnet. When the SOC is included, Fig. 5(d) shows the band structure of $P\uparrow$. The valley polarization direction is tuned by

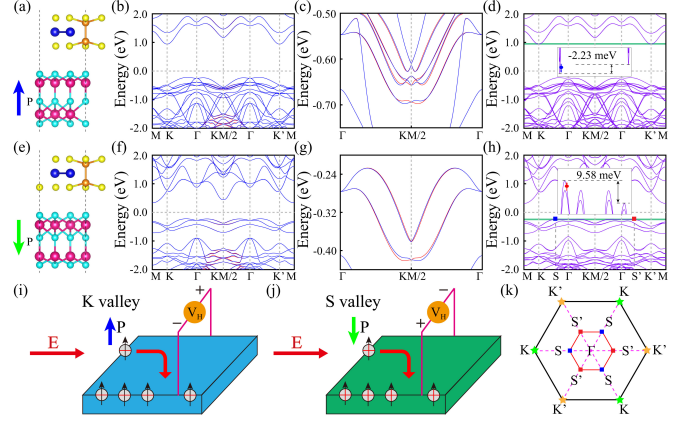


FIG. 5. (a, e) Side views of $VPSe_3/Al_2S_3$ heterostructures with the top-S configuration. (a) and (e) correspond to the upward and downward polarization of Al_2S_3 , respectively. (b, f) Spin-polarized band structure of $VPSe_3/Al_2S_3$ for (b) the $P\uparrow$ state and (f) the $P\downarrow$ state with the top-S configuration. The solid red and blue lines represent spin up and spin down bands, respectively. The (c) and (g) exhibit the enlarged view of the trion around $KM/2$ for (b) and (f). (d, h) Band structure of $VPSe_3/Al_2S_3$ heterostructures with the SOC effect for (d) the $P\uparrow$ state and (h) the $P\downarrow$ state with the top-S configuration. The green shading show the valley splitting. (i, j) Schematic diagrams of anomalous valley Hall effect in (i) the electron-doped monolayer $VPSe_3$ at the K valley, and (j) the hole-doped at the S valley, respectively. The electrons and holes are represented by the - and + symbol. The \uparrow and \downarrow denotes the spin up and spin down carriers, respectively. (k) Location of K/K' and S/S' valleys in the first Brillouin zone.

the Al_2S_3 , however, the magnitude has barely changed. When the ferroelectric polarization of Al_2S_3 becomes $P\downarrow$, as shown in Fig. 5(h), the valley splitting of 9.58 meV occurs at the VBM.

To understand the origin of VBM and CBM valley splitting, as shown in Fig. S6, we calculate the orbital-resolved band structure of top-S configuration $VPSe_3/Al_2S_3$. The CBM valley splitting comes from the Se atom liked monolayer $VPSe_3$, while the VBM valley splitting is contributed by $d_{x^2-y^2} + d_{xy}$ of V atoms. We uses $|\psi_v^\tau\rangle = \frac{1}{\sqrt{2}}(|d_{xy}\rangle + i\tau|d_{x^2-y^2}\rangle) \otimes |\uparrow\rangle$ as the orbital basis to construct an effective Hamiltonian. The derivation is consistent. Here, we only give the conclusion.

$$E_v^S - E_v^{S'} = i\langle d_{xy} | \hat{H}_{SOC}^0 | d_{x^2-y^2} \rangle - i\langle d_{x^2-y^2} | \hat{H}_{SOC}^0 | d_{xy} \rangle \approx 4\alpha, \quad (5)$$

where the $\hat{L}_z |d_{xy}\rangle = -2i\hbar |d_{x^2-y^2}\rangle$, $\hat{L}_z |d_{x^2-y^2}\rangle = 2i\hbar |d_{xy}\rangle$, and $\alpha = \lambda \langle d_{x^2-y^2} | \hat{S}_{z'} | d_{x^2-y^2} \rangle$.

It should be pointed out that the valley-dependent spin splitting occurs with the lower symmetry and SOC. Therefore, the anomalous valley Hall effect will be observed. As shown in Fig. 5(i), the spin down electron of K valley will be generated and accumulate on one boundary in electron doping condition for the $P\uparrow$. On the contrary, in the hole doping case, the spin up hole of S valley

will also be produced and accumulate on same boundary for the $P\downarrow$ [see Fig. 5(j)]. Furthermore, Fig. 5(k) shows the location of valley splits under two polarization states in the first Brillouin zone. All configurations of valley splitting are listed in Table I. Noted that the same phenomenon appears for other configurations, as shown in Fig. S4 and Fig. S5. It means that ferroelectric substrate Al_2S_3 can effectively tune the direction and magnitude of VPSe_3 valley polarization. More interestingly, the ferroelectric polarization can switch altermagnetism effect, which indicates the ferroelectric polarization is coupled to the altermagnetic spin splitting.

TABLE I. Calculate the valley splitting of different $\text{VPSe}_3/\text{Al}_2\text{S}_3$ heterostructure configurations, which is defined as valley splitting = $E_K - E_{K'}$.

	top-S top-Al hollow bridge			
$\text{VPSe}_3/\text{Al}_2\text{S}_3$ $P\uparrow$ (meV)	-2.23	-3.45	-3.13	-2.82
$\text{VPSe}_3/\text{Al}_2\text{S}_3$ $P\downarrow$ (meV)	9.58	9.15	8.74	8.96

V. CONCLUSION

In summary, we present a novel strategy to realizing altermagnet in 2D material. We use an electric field, Janus structure, and ferroelectric substrate to make the upper and lower atoms asymmetric, while the PT symmetry of the AFM state is broken, resulting in a transition to altermagnetic state. Based on the symmetry analysis and DFT calculation, the mechanism is proved to be feasible in monolayer VPSe_3 . The magnetic ground

state of monolayer VPSe_3 is an AFM state, which exhibits a spontaneous valley splitting of 2.91 meV. The electric field, the Janus structure, and the ferroelectric substrate can effectively break the PT symmetry, so that the band structure can exhibit spin splitting at the Γ - $\text{KM}/2$ - Γ path. It proves that multiple-physical-fields can transform monolayer VPSe_3 from AFM to altermagnetic state. Moreover, the electric field can adjust the magnitude of valley splitting, while the Janus structure can regulate both the magnitude and direction of valley splitting. For the ferroelectric substrate Al_2S_3 , the valley polarization direction is effectively tuned and the magnitude hardly changes under the $P\uparrow$. However, when the ferroelectric polarization of Al_2S_3 switches from $P\uparrow$ to $P\downarrow$, the valley splitting significantly increases. In addition, the ferroelectric polarization can switch altermagnetic effect and realize anomalous valley Hall effect. Our work not only provides a route to realize the altermagnet in 2D system, but also an efficient ways to tune valley splitting.

ACKNOWLEDGEMENTS

This work is supported by the National Natural Science Foundation of China (Grants No. 12474238, and No. 12004295). P. Li also acknowledge supports from the China's Postdoctoral Science Foundation funded project (Grant No. 2022M722547), the Fundamental Research Funds for the Central Universities (xxj03202205), and the Open Project of State Key Laboratory of Silicon and Advanced Semiconductor Materials (No. SKL2024-10), and the Open Project of State Key Laboratory of Surface Physics (No. KF2024_02).

-
- [1] H. Y. Ma, M. Hu, N. Li, J. Liu, W. Yao, J. F. Jia, and J. Liu, Multifunctional antiferromagnetic materials with giant piezomagnetism and noncollinear spin current, *Nat. Commun.* 12, 2846 (2021).
 - [2] L. Smejkal, J. Sinova, and T. Jungwirth, Beyond conventional ferromagnetism and antiferromagnetism: A phase with nonrelativistic spin and crystal rotation symmetry, *Phys. Rev. X* 12, 031042 (2022).
 - [3] L. Smejkal, J. Sinova, and T. Jungwirth, Emerging Research Landscape of Altermagnetism, *Phys. Rev. X* 12, 040501 (2022).
 - [4] Y. P. Zhu, X. Chen, X. R. Liu, Y. Liu, P. Liu, H. Zha, G. Qu, C. Hong, J. Li, Z. Jiang, X. M. Ma, Y. J. Hao, M. Y. Zhu, W. Liu, M. Zeng, S. Jayaram, M. Lenger, J. Ding, S. Mo, K. Tanaka, M. Arita, Z. Liu, M. Ye, D. Shen, J. Wrachtrup, Y. Huang, R. H. He, S. Qiao, Q. Liu, and C. Liu, Observation of plaid-like spin splitting in a noncoplanar antiferromagnet, *Nature*, 626, 523 (2024).
 - [5] J. Krempasky, L. Smejkal, S. W. DSouza, M. Hajlaoui, G. Springholz, K. Uhlirova, F. Alarab, P. C. Constantinou, V. Strocov, D. Usanov, W. R. Pudelko, R. G. Hernandez, A. B. Hellenes, Z. Jansa, H. Reichlova, Z. Soban, R. D. G. Betancourt, P. Wadley, J. Sinova, D. Kriegner, J. Minar, J. H. Dil, and T. Jungwirth, Altermagnetic lifting of Kramers spin degeneracy, *Nature*, 626, 517 (2024).
 - [6] L. Smejkal, A. B. Hellenes, R. G. Hernandez, J. Sinova, and T. Jungwirth, Giant and tunneling magnetoresistance in unconventional collinear antiferromagnets with nonrelativistic spin-momentum coupling, *Phys. Rev. X* 12, 011028 (2022).
 - [7] Z. Feng, X. Zhou, L. Smejkal, L. Wu, Z. Zhu, H. Guo, R. G. Hernandez, X. Wang, H. Yan, P. Qin, X. Zhang, H. Wu, H. Chen, Z. Meng, L. Liu, Z. Xia, J. Sinova, T. Jungwirth, and Z. Liu, An anomalous Hall effect in altermagnetic ruthenium dioxide, *Nat. Electron.* 5, 735 (2022).
 - [8] R. G. Hernandez, L. Smejkal, K. Vyborny, Y. Yahagi, J. Sinova, T. Jungwirth, and J. Zelezny, Efficient Electrical Spin Splitter Based on Nonrelativistic Collinear Antiferromagnetism, *Phys. Rev. Lett.* 126, 127701 (2021).
 - [9] S. Karube, T. Tanaka, D. Sugawara, N. Kadoguchi, M. Kohda, and J. Nitta, Observation of spin-splitter torque in collinear antiferromagnetic RuO_2 , *Phys. Rev. Lett.* 129, 137201 (2022).

- [10] H. Bai, L. Han, X. Y. Feng, Y. J. Zhou, R. X. Su, Q. Wang, L. Y. Liao, W. X. Zhu, X. Z. Chen, F. Pan, X. L. Fan, and C. Song, Observation of spin splitting torque in a collinear antiferromagnet RuO_2 , *Phys. Rev. Lett.* 128, 197202 (2022).
- [11] S. A. A. Ghorashi, T. L. Hughes, and J. Cano, Altermagnetic Routes to Majorana Modes in Zero Net Magnetization, *Phys. Rev. Lett.* 133, 106601 (2024).
- [12] H. G. Gill, and J. Linder, Superconductor-altermagnet memory functionality without stray fields, *Phys. Rev. B* 109, 134511 (2024).
- [13] X. Zhou, W. Feng, R. W. Zhang, L. Smejkal, J. Sinova, Y. Mokrousov, and Y. Yao, Crystal Thermal Transport in Altermagnetic RuO_2 , *Phys. Rev. Lett.* 132, 056701 (2024).
- [14] J. Ding, Z. Jiang, X. Chen, Z. Tao, Z. Liu, T. Li, J. Liu, J. Sun, J. Cheng, J. Liu, Y. Yang, R. Zhang, L. Deng, W. Jing, Y. Huang, Y. Shi, M. Ye, S. Qiao, Y. Wang, Y. Guo, D. Feng, and D. Shen, Large Band Splitting in g-Wave Altermagnet CrSb , *Phys. Rev. Lett.* 133, 206401 (2024).
- [15] Z. Q. Wang, Z. Q. Li, L. Sun, Z. Y. Zhang, K. He, H. Niu, J. Cheng, M. Yang, X. Yang, G. Chen, Z. Yuan, H. F. Ding, and B. F. Miao, Inverse Spin Hall Effect Dominated Spin-Charge Conversion in (101) and (110)-Oriented RuO_2 Films, *Phys. Rev. Lett.* 133, 046701 (2024).
- [16] L. Bai, W. Feng, S. Liu, L. Sejkal, Y. Mokrousov, and Y. Yao, Altermagnetism: Exploring New Frontiers in Magnetism and Spintronics, *Adv. Funct. Mater.* 34, 2409327 (2024).
- [17] D. Xiao, W. Yao, and Q. Niu, Valley-Contrasting Physics in Graphene: Magnetic Moment and Topological Transport, *Phys. Rev. Lett.* 99, 236809 (2007).
- [18] T. Cao, G. Wang, W. Han, H. Ye, C. Zhu, J. Shi, Q. Niu, P. Tan, E. Wang, B. Liu, and J. Feng, Valley-selective circular dichroism of monolayer molybdenum disulphide, *Nat. Commun.* 3, 887 (2012).
- [19] K. F. Mak, K. He, J. Shan, and T. F. Heinz, Control of valley polarization in monolayer MoS_2 by optical helicity, *Nat. Nanotechnol.* 7, 494 (2012).
- [20] H. Zeng, J. Dai, W. Yao, D. Xiao, and X. Cui, Valley polarization in MoS_2 monolayers by optical pumping, *Nat. Nanotechnol.* 7, 490 (2012).
- [21] W. Y. Tong, S. J. Gong, X. Wan, and C. G. Duan, Concepts of ferrovalley material and anomalous valley Hall effect, *Nat. Commun.* 7, 13612 (2016).
- [22] R. Peng, Y. Ma, X. Xu, Z. He, B. Huang, and Y. Dai, Intrinsic anomalous valley Hall effect in single-layer Nb_3I_8 , *Phys. Rev. B* 102, 035412 (2020).
- [23] K. Wang, Y. Li, H. Mei, P. Li, and Z. X. Guo, Quantum anomalous Hall and valley quantum anomalous Hall effects in two-dimensional d^0 orbital XY monolayers, *Phys. Rev. Mater.* 6, 044202 (2022).
- [24] P. Li, C. Wu, C. Peng, M. Yang, and W. Xun, Multi-field tunable valley splitting in two-dimensional MXene Cr_2COOH , *Phys. Rev. B* 108, 195424 (2023).
- [25] P. Li, X. Yang, Q. S. Jiang, Y. Z. Wu, and W. Xun, Built-in electric field and strain tunable valley-related multiple topological phase transitions in VSiXN_4 ($X = \text{C}, \text{Si}, \text{Ge}, \text{Sn}, \text{Pb}$) monolayers, *Phys. Rev. Mater.* 7, 064002 (2023).
- [26] P. Li, B. Liu, S. Chen, W. X. Zhang, and Z. X. Guo, Progress on two-dimensional ferrovalley materials, *Chin. Phys. B* 33, 017505 (2024).
- [27] Y. Wu, J. Tong, L. Deng, F. Luo, F. Tian, G. Qin, and X. Zhang, Coexisting Ferroelectric and Ferrovalley Polarizations in Bilayer Stacked Magnetic Semiconductors, *Nano Lett.* 23, 6226 (2023).
- [28] W. Xun, C. Wu, H. Sun, W. Zhang, Y. Z. Wu, and P. Li, Coexisting Magnetism, Ferroelectric, and Ferrovalley Multiferroic in Stacking-Dependent Two-Dimensional Materials, *Nano Lett.* 24, 3541 (2024).
- [29] S. D. Guo, L. Zhang, Y. Zhang, P. Li, and G. Wang, Large spontaneous valley polarization and anomalous valley Hall effect in antiferromagnetic monolayer Fe_2CF_2 , *Phys. Rev. B* 110, 024416 (2024).
- [30] X. W. Shen, W. Y. Tong, S. J. Gong, and C. G. Duan, Electrically tunable polarizer based on 2D orthorhombic ferrovalley materials, *2D Mater.* 5, 011001 (2017).
- [31] P. E. Blochl, Projector augmented-wave method, *Phys. Rev. B* 50, 17953 (1994).
- [32] G. Kresse, and J. Furthmuller, Efficient iterative schemes for ab initio total-energy calculations using a plane-wave basis set, *Phys. Rev. B* 54, 11169 (1996).
- [33] J. P. Perdew, K. Burke, and M. Ernzerhof, Generalized Gradient Approximation Made Simple, *Phys. Rev. Lett.* 77, 3865 (1996).
- [34] H. P. Wang, W. Luo, and H. J. Xiang, Prediction of high-temperature quantum anomalous Hall effect in two-dimensional transition-metal oxides, *Phys. Rev. B* 95, 125430 (2017).
- [35] S. Grimme, J. Antony, S. Ehrlich, and H. Krieg, A consistent and accurate ab initio parameterization of density functional dispersion correction (DFT-D) for the 94 elements H-Pu, *J. Chem. Phys.* 132, 154104 (2010).
- [36] A. A. Mostofi, J. R. Yates, Y. S. Lee, I. Souza, D. Vanderbilt, and N. Marzari, wannier90: A tool for obtaining maximally-localised Wannier functions, *Comput. Phys. Commun.* 178, 685 (2008).
- [37] A. A. Mostofi, J. R. Yates, G. Pizzi, Y. S. Lee, I. Souza, D. Vanderbilt, and N. Marzari, An updated version of wannier90: A tool for obtaining maximally-localised Wannier functions, *Comput. Phys. Commun.* 185, 2309 (2014).
- [38] C. Gong, L. Li, Z. Li, H. Ji, A. Stern, Y. Xia, T. Cao, W. Bao, C. Wang, Y. Wang, Z. Q. Qiu, R. J. Cava, S. G. Louie, J. Xia, and X. Zhang, Discovery of intrinsic ferromagnetism in two-dimensional van der Waals crystals, *Nature*, 546, 265 (2017).
- [39] B. Huang, G. Clark, E. N. Moratalla, D. R. Klein, R. Cheng, K. L. Seyler, D. Zhong, E. Schmidgall, M. A. McGuire, D. H. Cobden, W. Yao, D. Xiao, P. J. Herrero, and X. Xu, Layer-dependent ferromagnetism in a van der Waals crystal down to the monolayer limit, *Nature* 546, 270 (2017).
- [40] Q. Lu, P. Li, Z. Guo, G. Dong, B. Peng, X. Zha, T. Min, Z. Zhou, and M. Liu, Giant Tunable Spin Hall Angle in Sputtered Bi_2Se_3 Controlled by an Electric Field, *Nat. Commun.* 13, 1650 (2022).
- [41] P. Li, X. S. Zhou, and Z. Guo, Intriguing Magnetoelectric Effect in Two-dimensional Ferromagnetic Perovskite Oxide Ferroelectric Heterostructure, *npj Comput. Mater.* 8, 20 (2022).
- [42] L. Zhang, J. Yu, M. Yang, Q. Xie, H. Peng, and Z. Liu, Janus graphene from asymmetric two-dimensional chemistry, *Nat. Commun.* 4, 1443 (2013).
- [43] A. Y. Lu, H. Zhu, J. Xiao, C. P. Chuu, Y. Han, M. H. Chiu, C. C. Cheng, C. W. Yang, K. H. Wei, Y. Yang, Y.

- Wang, D. Sokaras, D. Nordlund, P. Yang, D. A. Muller, M. Y. Chou, X. Zhang, and L. J. Li, Janus monolayers of transition metal dichalcogenides, *Nat. Nanotechnol.* 12, 744 (2017).
- [44] Y. C. Lin, C. Liu, Y. Yu, E. Zarkadoula, M. Yoon, A. A. Puretzky, L. Liang, X. Kong, Y. Gu, A. Strasser, H. M. Meyer III, M. Lorenz, M. F. Chisholm, I. N. Ivanov, C. M. Rouleau, G. Duscher, K. Xiao, and D. B. Gehegan, Low Energy Implantation into Transition-Metal Dichalcogenide Monolayers to Form Janus Structures, *ACS Nano* 14, 3896 (2020).
- [45] H. Tang, W. Li, L. Pan, K. Tu, F. Du, T. Qiu, J. Yang, C. P. Cullen, N. McEvoy, C. Zhang, and A Robust, Freestanding MXene-Sulfur Conductive Paper for Long-Lifetime Li-S Batteries, *Adv. Funct. Mater.* 29, 1901907 (2019).